Received xxx; | Revised xxx; | Accepted xxx

DOI: xxx/xxxx

ORIGINAL ARTICLE

Time-Dependent Simulation of Ion Stopping: Charge Transfer and Electronic Excitations

N. Schlünzen*[1] | K. Balzer[2] | M. Bonitz[1] | L. Deuchler[1] | E. Pehlke[1]

[1]Institut für Theoretische Physik und Astrophysik,
Christian-Albrechts-Universität zu Kiel,
Leibnizstraße 15, 24098 Kiel, Germany
[2]Rechenzentrum,
Christian-Albrechts-Universität zu Kiel,
24098 Kiel, Germany

Correspondence
*Email: schluenzen@theo-physik.uni-kiel.de

The energy loss of charged particles in matter has been studied for many decades, both, analytically and via computer simulations. While the regime of high projectile energies is well understood, low energy stopping in solids is more challenging due to the importance of non-adiabatic effects and electronic correlations. Here we consider two problems: the charge transfer between substrate and projectile and the role of electronic correlations, specifically formation of doubly occupied lattice sites in the material during the stopping process. The former problem is treated by time-dependent density functional theory simulations and the latter by nonequilibrium Green functions.

KEYWORDS:
stopping power, TDDFT simulations, Nonequlibrium Green functions, charge transfer, doublon formation

1 | INTRODUCTION

The impact of ions on a solid surface is of prime importance for plasma physics and surface science and has been studied for decades, both, experimentally and theoretically. The theoretical approaches include scattering theory[1] or uniform electron gas models[2]. Here the primary input is the dynamic inverse dielectric function (or dynamic structure factor, DSF) for which electron gas models or recently developed quantum Monte Carlo methods[3] can be applied. Recently, also *ab-initio* simulations of ion stopping based on time-dependent density functional theory (TDDFT) were reported for metals[4], semimetals[5] or boron nitride and graphene sheets[6] and other materials. These simulations account primarily for valence-electron excitation. Good results for the stopping power of high energy ions in matter are also provided by the SRIM code[7] that uses the binary collision approximation in combination with an averaging over a large range of experimental situations. Stopping power simulations have also been extensively applied for plasmas using kinetic equations. Here, again, the energy loss is usually computed by integrating of the DSF of the plasma which can be understood as a linear-response approach. At the same time, also time-resolved simulations have been performed based on quantum kinetic theory[8],[9] which allow one to go beyond the linear response approximation. This is of particular importance in case of strong excitation or for the treatment of fast non-adiabatic processes in the target.

Aside from high density plasmas (warm dense matter), e.g. Refs. 10 and 11, ion stopping is also of central relevance for low-temperature plasmas in contact with a solid surface. This latter system is in the focus of the present paper. In these plasmas most of the ions are usually in equilibrium with the neutral gas and are at room temperature. In addition, close to the surface (in the plasma sheath) ions may be accelerated by the sheath electric field up to keV energies, for a recent overview on plasma–surface simulations see Ref. 12. Even though the overall behavior of the stopping power as a function of ion impact energy is understood, for low-temperature plasmas special questions remain open. This includes: how does charge transfer between substrate and ion occur (neutralization of projectile)? How does it depend on the impact energy and on the substrate material? In what distance from the target does it occur? Furthermore, how does the stopping behavior change in the case of nontrivial

targets that either have a complicated surface morphology, nanostructuring or exhibit strong electronic correlations? Answers to these questions are not only of fundamental interest but are also important for applications as they may give rise to new plasma–surface combinations with non-traditional properties.

The goal of the present paper is to address some of these questions that are of relevance for low-temperature plasmas. We present time-resolved non-adiabatic simulations of ion stopping that are capable of resolving the electronic processes in the projectile and in the target. In particular, we concentrate on two questions. The first is the charge transfer between a metallic substrate and an incoming proton which we treat via time-dependent density functional theory, cf. Sec. 2. The second question is the change of stopping power in correlated nano-scale materials. Here we apply nonequilibrium Green functions (NEGF)–Ehrenfest simulations, extending the recent work of Balzer *et al.* [13,14]. The NEGF approach is introduced in Sec. 3 and applied to finite graphene-type Hubbard clusters. Finally, in Sec. 4 we discuss how the two complementary approaches might be combined in the future in order to achieve a comprehensive description of ion and electron dynamics at the plasma–solid interface.

2 | TIME-DEPENDENT DENSITY FUNCTIONAL THEORY SIMULATIONS OF CHARGE TRANSFER AND ION STOPPING

In this section we present *ab-initio* molecular dynamics (MD) simulations for the neutralization of an ion, H^+, incident on a simple metal surface, Al(111), which we have carried through using the Octopus code [15–17]. The metal substrate is represented by a cluster. The coupled system of the ions and the electrons is described in an approximate way by using Ehrenfest dynamics [15,18]. The Al atomic coordinates will be kept fixed during the time-dependent simulation, but this restriction could easily be lifted without any significant additional computational effort. The electrons are described within time-dependent density functional theory (TDDFT) [15,19,20]. The time-dependent Kohn–Sham equations, which in case of a local potential v read (in atomic units)

$$\mathrm{i}\frac{\partial \psi_j(\mathbf{r},t)}{\partial t} = -\frac{1}{2}\nabla^2\psi_j(\mathbf{r},t) + \left(\mathrm{v}(\mathbf{r},t) + \int \mathrm{d}^3\mathbf{r}'\,\frac{\mathrm{n}(\mathbf{r}',t)}{|\mathbf{r}-\mathbf{r}'|} + \mathrm{v}_{\mathrm{XC}}(\mathbf{r},t)\right)\psi_j(\mathbf{r},t)\,, \tag{1}$$

are integrated together with the Ehrenfest equation of motion. The electron density is calculated from the sum over the probability densities of the time-dependent Kohn–Sham states that are occupied in the initial state, which itself is constructed by combining the separately calculated electronic Kohn–Sham ground-states of the metal atom cluster and the incident particle. The adiabatic approximation is applied to the exchange–correlation (XC) potential v_{XC}, and, in addition, an approximate XC functional from ground-state DFT is used:

$$v_{\mathrm{XC}}(\mathbf{r},t) \approx v_{\mathrm{XC}}^{\mathrm{approx}}([n(.,t)],\mathbf{r})\,. \tag{2}$$

In case of a proton incident on a metal surface, the electronic system is initially strongly locally excited. This is different from the case of an atom, *e.g.* H^0, scattered at the surface [21]. The adiabatic approximation of the XC potential will be a more serious approximation in case of the strongly locally electronically excited system. In particular, Auger transitions are not expected to be accounted for [22,23]. However, this is not a major restriction in case of the present simulations, because Merino *et al.* [24] have concluded from their study using a model Hamiltonian that at the low H^+ kinetic energies considered here (below keV) the charge transfer is dominated by resonant processes. Finally, we note that the TDDFT-MD simulations we present below refer to the valence electrons only. The core electronic states of the metal atoms have been incorporated into an ionic pseudopotential. Moreover, also the s-wavefunction of the H-atom is pseudoized.

Important insight into proton neutralization at Al surfaces has been achieved by various authors using rate equations [25,26] or (Newns–Anderson-type) model Hamiltonians [24,27–30]. While strong correlation effects can be incorporated into model Hamiltonians, the advantage of the direct simulation of the charge transfer process using a TDDFT code like Octopus lies in the *ab-initio* determination of the time-dependent electron density (*i.e.* screening and charge transfer), the effective potential, and hence the time-dependent electron tunneling probabilities.

TDDFT-MD simulations of ions accounting for resonant charge transfer have been carried out by other authors before, *e.g.* for the interaction of Li^+ with an Al_{58}-cluster by Moss *et al.* [31], for a proton scattered at a Li_4-cluster by Castro *et al.* [32], and collisions with carbon nanostructures by Krasheninnikov *et al.* [33], or DNA fragments by Seraide *et al.* [34], or graphene fragments by Bubin *et al.* [35], or graphene and boron nitride by Zhao *et al.* [36], and for Cl^- incident on a $MoSe_2$ monolayer by Wang *et al.* [37]. This has lead to many significant scientific advances. However, there are open questions concerning *e.g.* the resonant charge transfer in particular at low kinetic energies and the effect of the approximation to the XC-potential [38,39]. Moreover, technological advances allow for the treatment of more extended systems. Here we present a TDDFT-MD simulation

of the charge transfer and energy dissipation for an H^+ ion with initial kinetic energy 2 eV ... 50 eV incident on an Al(111) metal surface (modeled by a cluster), and compare to the energy dissipation in case of an incident H-atom.

Technical details of the TDDFT-MD simulations are summarized below.

2.1 | Computational details

The Octopus code (version 6) by Rubio *et al.*[15–17] has been employed for all TDDFT-MD simulations presented in this paper. The adiabatic approximation is applied to v_{xc}, together with the Perdew–Burke–Ernzerhof (PBE) generalized gradient approximation for exchange and correlation from ground-state DFT (PBE-GGA)[40]. The Al(111) surface is modeled by a cluster containing either 172 Al-atoms (for H^+ incident at the Al(111) hollow site) or 188 Al-atoms (for H^+ incident at the on-top site). The Al-clusters have been created by cutting out half-spheres from a (111)-oriented substrate with lattice constant of 4.047 Å as determined from ground-state DFT calculations with the convergence parameters and pseudopotential as described below. The uppermost Al-layer has been fixed and an ionic relaxation of the remaining Al-atoms has been performed. The simulation has been performed inside a user-defined region (see Fig. 1 (a)) that fits into a cube with edge size 60 bohr, and a minimum distance between atoms and the boundary of the user-defined region of 12 bohr. The FFT for solving the Poisson equation requires a box with twice the edge length of the cube described above. Ions are represented by norm-conserving Troullier–Martins pseudopotentials[41] created with FHIPP[42]. In case of the Al atom, ten electrons are treated as frozen-in core states. The non-local pseudopotential is p-local in case of Al and s-local in case of H. The following cut-off radii have been used for the creation of the pseudpotentials: $r^{Al}_{1s} = 1.791$ bohr, $r^{Al}_{2p} = 1.974$ bohr, $r^{Al}_{3d} = 2.124$ bohr, $r^{H}_{1s} = 1.276$ bohr, $r^{H}_{2p} = 1.276$ bohr. Fourier components of the pseudopotentials beyond the cut-off determined by the real-space mesh size are filtered using the method of Tafipolsky and Schmid[43] as supplied within Octopus. The Kohn–Sham wavefunctions are sampled on a real-space grid. We have used a spacing $\Delta x = 0.5$ bohr. As a test, we have carried through simulations with either smaller spacings ≥ 0.4 bohr or larger cluster (302 atoms for H^+ towards the on-top position). The electronic ground state of the Al-cluster has been determined using a Methfessel–Paxton smearing[44] with a small smearing parameter of 20 meV.

In case of the H^+ projectile, the bare H-pseudopotential has been added to the simulation box. In case of the H^0 projectile, in addition the spin-polarized ground-state Kohn–Sham wavefunction of the H-atom has been calculated and added to the set of wavefunctions. The initial distance between target and projectile is set to 16 bohr. An initial velocity has been assigned to the projectile, corresponding to a kinetic energy of 2 eV, 10 eV or 50 eV. The initial-state Kohn–Sham wavefunction of the H-atom has been multiplied with a boost phase factor[22,45]. The Al atomic positions were kept fixed during the simulations. A time step of 0.02 atomic time units (0.5 attoseconds) has been used for the propagation of the Kohn–Sham wavefunctions. The exponent in the propagator is approximated using the exponential midpoint rule, and a fourth-order Taylor expansion of the exponential is used as implemented in Octopus[46].

2.2 | Charge transfer H^+/Al(111)

The charge transfer from the Al-substrate to the H^+ projectile as derived from the TDDFT-MD simulations is shown in Fig. 1 (b) for the initial condition that the projectile is incident on the on top-site of the Al(111) surface. Only the incoming part of the trajectory—before the H–Al head-on collision—is analyzed. As the eigenvalue of the hydrogen 1s level is located inside the valence band of bulk Al, resonant neutralization via elastic tunneling of the electron from the metal to the proton is possible[24]. In order to quantify the charge transfer $q(t)$ to the incident H^+ ion we project the time-dependent Kohn–Sham wavefunctions $|\psi_j(t)\rangle$ onto the H 1s-orbital $|1s\rangle$. Including the occupation f_j this yields the local charge of the H-ion

$$q(t) = \sum_j f_j |\langle 1s|\psi_j(t)\rangle|^2 \,. \tag{3}$$

In Fig. 1 (b) the transferred charge is plotted as a function of the distance of the projectile from the Al-surface. The neutralization of the proton occurs at a distance between 4 bohr and 6 bohr in front of the surface, depending on proton velocity. This is consistent with the respective distance obtained by Jouin and Gutierrez[26]. The H^+ neutralization has been reported in the literature[29] to be very efficient. As the slower projectile spends a longer time at a certain separation in front of the metal surface, the neutralization of the slower particle occurs at larger separation from the surface. The charge on the H finally exceeds a value of 1.0. Negatively charged hydrogen is well known, *e.g.* in case of metal hydrides[48]. The quantitative value (as compared to other definitions of local ionic charges) may be partially affected by the overlap of the H1s wavefunction with the electronic states of the Al-cluster. The data may be useful for the parametrization of the H–Al interaction in many-particle model Hamiltonians.

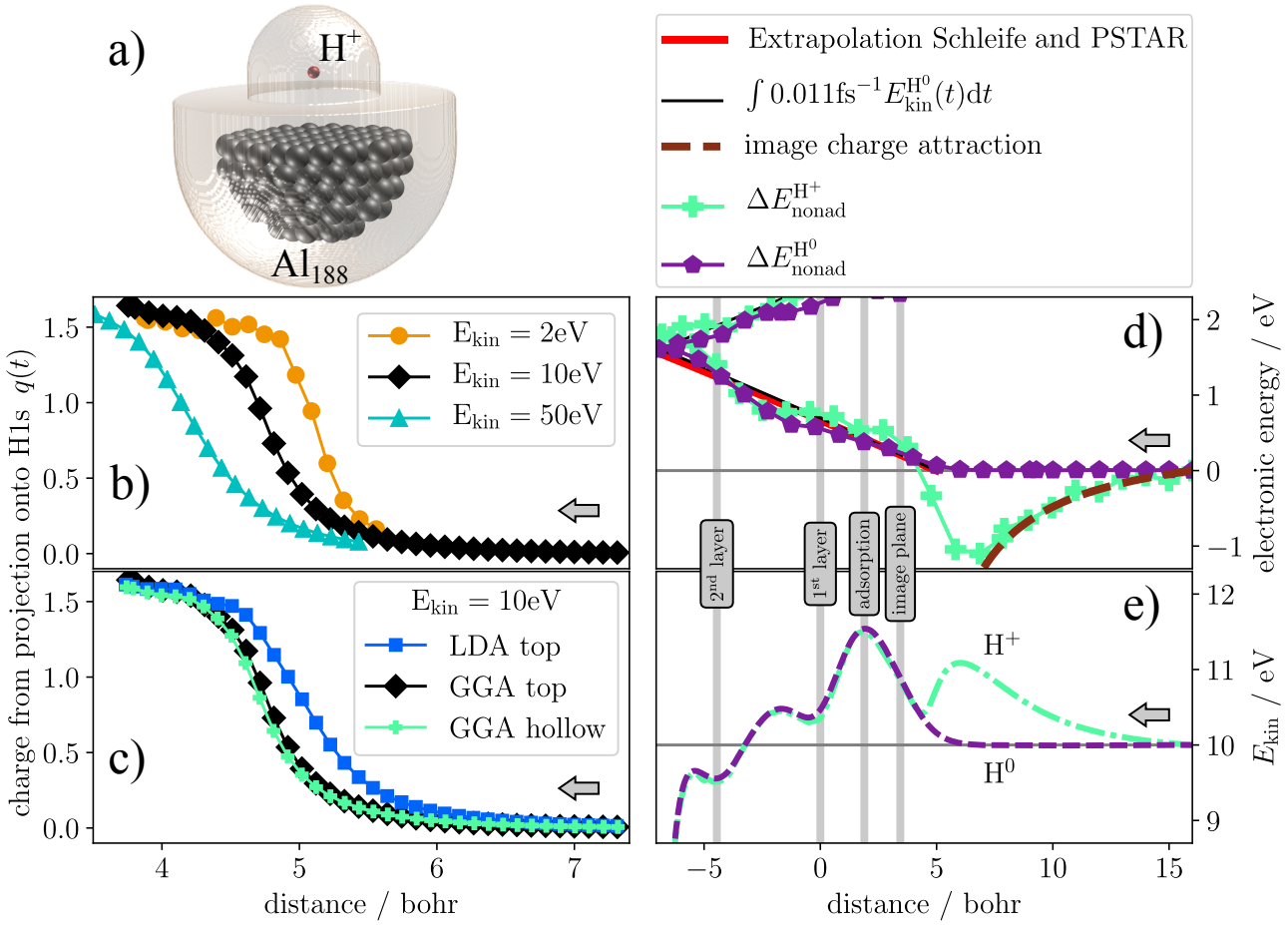

FIGURE 1 **a)** Visualization of Al-cluster and simulation box in case of H–Al on-top collision; graphic produced using the vmd software[47]. **b)** Charge transfer from the Al(111) target to the H^+projectile incident on an Al on-top site as obtained from the TDDFT-MD simulations (Eq. 3). The uppermost Al-layer is located at $z = 0$ bohr. **c)** Comparison of charge transfer for H^+-projectile incident on an Al-hollow or on-top site and comparison between GGA and LDA results. **d)** Comparison of the variation of the electronic excitation energy (Eqs. 4 and 5) and **e)** the kinetic energy of the H^+ or H^0 projectile incident on the Al(111) fcc hollow-site. The H penetrates the surface and propagates through the first two layers inside the Al-cluster until it is reflected at the third Al-layer.

As can be read from the results for the charge transfer to a proton with initial kinetic energy of 10 eV shown in Fig. 1 (c), the charge-transfer dynamics is rather insensitive to the point of incidence on the Al-surface. This was to be expected in view of the small corrugation of the effective potential and electron density far above the metal surface layer. However, we note a significant sensitivity of the charge-transfer dynamics on the choice of the approximation—here LDA vs. PBE-GGA—applied to the electronic ground-state XC-energy functional. We suggest that this may be due to differences in the description of the electronic ground state of the H-atom.

There is a well-known difficulty to describe long-range correlations with semilocal approximations for the XC energy functional in ground-state calculations[49]. *E.g.* when describing the dissociation of H_2 with a semilocal XC-functional, an artificial transition to a spin-polarized system is in general used to describe total energies at large atom separation[49,50]. In time-dependent simulations of H^0 incident on a metal surface, the H^0 atom has been assumed to be electronically spin-polarized at large separations from the surface and loses spin polarization when interacting with the surface[51,52]. We also use an initially spin-polarized H^0-atom in the present simulations in Sect. 2.3. In case of H^+ incident on the Al-cluster in the present calculation the initial configuration is spin-unpolarized and there is no term in the Hamiltonian that could break this symmetry during time evolution. We therefore suspect that the exchange-correlation effects are not well accounted for by the present spin-unpolarized semilocal

approximation to v_{XC}, and more advanced approximations would be desirable [49]. For the model-Hamiltonian calculations, the problem of correlation has been approached using *e.g.* as approximation for the correlation in multiple-level systems $U \to \infty$ [30].

It is argued that no electron–electron relaxation (Auger effect) occurs when the present adiabatic XC-functionals are employed [22,23]. Theoretical work on the He^+/Al system shows that in case of the projectile velocity range applied here, the Auger channel is the relevant one in order to be able to describe the experiment [53–56]. First test calculations within the framework described above for a He^+ ion ($E_{kin} = 2$ H) incident on an Al(111) surface, confirm that Auger processes do not show in the calculations performed using an adiabatic GGA XC-functional. Hence, other methods beyond the TDDFT-MD with adiabatic GGA have to be used if Auger transitions are to be considered.

2.3 | Energy dissipation for H^+, H^0 projectiles penetrating the Al-surface

TDDFT-MD simulations of an H^+ or an H^0 projectile starting 16 bohr above the hollow site of the Al(111) surface facet of the Al-cluster with an initial kinetic energy of 10 eV show—in agreement with similar previous TDDFT-MD simulations for H^0 by Lindenblatt *et al.* [21,57]—that the projectile (in case of H^+ after neutralization) penetrates the Al-surface. It propagates through the top two metal layers before it is reflected at the third atomic layer in a head-on collision. In Fig. 1 (d) the variation of the electronic excitation energy with respect to its initial value is plotted versus the distance of the projectile from the surface (defined by the position of the top layer Al atoms). In case of the uncharged H^0 this equals the electronically nonadiabatic energy, which is defined by the difference between the electronic energy in the time-dependent simulation and the energy of the electronic ground state at frozen-in atomic coordinates $R(t) = (\mathbf{R}_1(t), ..., \mathbf{R}_N(t))$:

$$\Delta E^{H^0}_{nonad} := E_{td}(t) - E_{gs}(R(t)) \, . \tag{4}$$

In case of a proton incident on the surface, in addition the energy needed to ionize an H-atom, *i.e.* to transfer one electron from the H^0-atom to the Al-cluster, has been subtracted for the sake of easier comparison to the case of H^0:

$$\Delta E^{H^+}_{nonad} := E_{td}(t) - E_{gs}(R(t)) - (E_{ion}(H) - W_A(\mathrm{Al-cluster})) \, . \tag{5}$$

All energies refer to DFT calculations with PBE-GGA applied to v_{XC}. In Fig. 1 (e) the kinetic energies of the H^+ and H^0 projectiles are visualized. The neutral H^0 projectile approaches the surface, accelerates inside the chemisorption well and transverses the adsorption position (at 1.89 bohr) where it gains the adsorption energy of 1.93 eV. This results in an increase of the kinetic energy of the projectile, however, part of the kinetic energy of the projectile is dissipated into electron–hole pair excitations [21]. The charged projectile H^+ is accelerated towards the surface due to the image-charge attraction [58]. The image plane of Al(111) is located at $z_{image} = 3.49$ bohr in front of the surface, according to Ref. 59. The image-charge potential $1/(4(z - z_{image}))$ that would be induced in case of an infinitely large surface slab is included in Fig.1 (d) by the brown dashed curve. In case of the finite cluster utilized here, the attractive potential will deviate from the simple image-potential form. The kinetic energy gain of about 0.54 eV due to attraction by the image charge of a proton starting infinitely far away from a plane surface and reaching a surface separation of 16 bohr is not accounted for in our calculation. As can be seen by comparing Figs. 1 (d) and (e), while the kinetic energy increases due to image-charge attraction, the electronic excitation energy decreases by about the same amount (brown dashed curve in Fig. 1 (d)). This is in line with conservation of total energy. Note that E_{gs} in Eq. 5 refers to the electronic ground state, *i.e.* an uncharged H^0. Thus the change of electrostatic energy due to polarization of the Al-cluster by the proton is included in $\Delta E^{H^+}_{nonad}$. At a surface separation between 4.5 bohr and 6.0 bohr, the partially charged H^+ loses kinetic energy. This region coincides with the region where the charge transfer occurs (see Fig. 1 (c)). The deacceleration of the projectile is ascribed to Coulomb repulsion between the projectile and the Al-cluster. In case of an infinitely large substrate and in the adiabatic limit the charge transferred to the projectile will, in the electrostatic case, come from infinity. Hence we have to be aware that the above Coulomb repulsion effect will be limited to the finite-size clusters. The cluster-size convergence is expected to be slow. Thus we cannot easily generalize the result of the rather similar variation of the kinetic energy of the H^+ and H^0 projectile at distances smaller than 4.5 bohr from our cluster calculation to the case of a metallic half space. However, as far as the interaction with the Al-cluster used in the simulations is concerned, the H^+ loses its charge in front of the surface and the variation of the electronic excitation energy comes out very similar when the projectile propagates within the metal cluster. This is in line with the observation that final projectile charges do not depend on the charge state of the incident particle for the given H^+/Al system and velocity range by *e.g.* Zimny *et al.* [25], Jouin *et al.* [26] and Torralba *et al.* [29]. The similar behavior between H^+ and H^0 incident on *e.g.* a graphene sheet has been noted before in TDDFT-MD calculations by Krasheninnikov *et al.* [33].

For clarity we point out that, while not immediately deducable from Fig. 1 (d) and (e), the neutralization of the H^+ in front of the surface is associated with a strong energy transfer into hole excitations of the metal substrate as the hole tunnels from the proton into the metal.

Stopping power for protons in bulk Al has been discussed and analyzed in detail by several authors using TDDFT-dynamics [60–62], or linear-response theory [63,64]. A neutral hydrogen atom impinging on the Al(111) surface and penetrating into the crystal has been studied before in Refs. 21 and 57. Theory for bulk electronic stopping agrees with experimental data, especially in the low-energy range subject to the present investigation. For comparison, in Fig. 1 (d) we include the stopping power derived from a linear-friction ansatz [21] (black curve) as well as an extrapolation of data from Schleife *et al.* [61] and PSTAR [65] (red curve). The starting point of both curves is chosen to coincide with the commencing electron–hole pair creation. Thus we agree with previous work [21,60–64] that electronic stopping of Hydrogen (after neutralization) within the Al-metal can reliably be simulated by TDDFT. At the same time, many questions remain to be solved, for a discussion see Sec. 4.

3 | NONEQUILIBRIUM GREEN FUNCTIONS–EHRENFEST APPROACH TO ION STOPPING IN CORRELATED MATERIALS

3.1 | Theory overview

A method that allows for a systematic treatment of electronic correlations in a solid-state material and, at the same time, of inhomogeneity effects induced by an external excitation are (real-time) nonequilibrium Green functions (NEGF) [66–69]. The central quantity is the one-particle NEGF

$$G_{ij\sigma}(t,t') = -\mathrm{i}\hbar\langle T_C c_{i\sigma}(t) c^\dagger_{j\sigma}(t')\rangle\,, \tag{6}$$

which appears as a two-time generalization of the one-particle density matrix $\rho_{ij\sigma}(t) = -\frac{\mathrm{i}}{\hbar}G_{ji\sigma}(t,t^+)$, where the notation t^+ means $t = t + \epsilon$ with $\epsilon_{>0} \to 0$, and G determines all time-dependent one-particle observables. In the definition of the NEGF, $c^\dagger_{i\sigma}$ ($c_{i\sigma}$) are creation (annihilation) operators in the Heisenberg picture for electrons in a single-particle orbital $|i\rangle$ with spin projection σ, and the expectation value is computed with the equilibrium density operator of the system. Furthermore, times are running along the Keldysh contour $\mathcal{C}$, with T_C denoting ordering of operators on $\mathcal{C}$ [67,70,71]. The equations of motion for the NEGF are the two-time Keldysh–Kadanoff–Baym equations (KBE) [67]

$$\sum_k \left[\mathrm{i}\hbar\partial_t\delta_{ik} - \bar{h}_{ik\sigma}(t)\right] G_{kj\sigma}(t,t') = \delta_C(t-t')\delta_{ij} + \sum_k \int_C \mathrm{d}s\, \Sigma_{ik\sigma}(t,s) G_{kj\sigma}(s,t')\,, \tag{7}$$

$$\sum_k G_{ik\sigma}(t,t') \left[-\mathrm{i}\hbar\overleftarrow{\partial}_{t'}\delta_{kj} - \bar{h}_{kj\sigma}(t')\right] = \delta_C(t-t')\delta_{ij} + \sum_k \int_C \mathrm{d}s\, G_{kj\sigma}(t,s)\Sigma_{ik\sigma}(s,t')\,, \tag{8}$$

a set of two integro-differential equations, where the Hamiltonian $\bar{h}(t)$ contains the one-particle kinetic, potential and mean-field energy, whereas correlation effects are contained in the two-time selfenergy $\Sigma(t,t')$ that can be approximated as a functional of the NEGF according to a diagrammatic many-body perturbation expansion. Note, that in the given form of the KBE we do not consider spin changes and assume a paramagnetic system.

As an approximation for the selfenergy beyond the Hartree–Fock (HF) level (for which $\Sigma = 0$ and mean-field contributions are incorporated in $\bar{h}(t)$), we consider in the present work the second-order Born (2B) approximation [66,67], which conserves total energy, particle number and momentum and is specified in Eq. (12) below for the case of a local Hubbard-type interaction. For more advanced expressions for the selfenergy, such as GW, T matrix or third order, see, e.g., Refs. 72,73. In addition to the use of the 2B approximation, we simplify the solution of the KBE in one of two ways:

(i) we apply the generalized Kadanoff–Baym ansatz (GKBA) with HF propagators, as proposed in Ref. 74, to reduce the computational effort of solving the KBE (7) and (8) from a scaling $\sim T^3_{\mathrm{tot}}$ with the total simulation duration to $\sim T^2_{\mathrm{tot}}$, see Ref. 75 for details,

(ii) we consider the selfenergy to be local in space, $\Sigma_{ij\sigma}(t,t') = \delta_{ij}\Sigma_{i\sigma}(t,t')$, for which the KBE can be solved very efficiently using the auxiliary-Hamiltonian representation introduced in Ref. 76.

Both strategies allow us to reach sufficiently long propagation times that are needed to treat electronic excitations during charged-particle stopping scenarios with sub-keV impact energies. To include an external moving charge (projectile) into the KBE simulations, we choose an NEGF–Ehrenfest approach which was first presented in Ref. 13 and applied in Refs. 14 and 77. In the

course of this, the trajectory $r(t)$ of the projectile is calculated on the fly by Ehrenfest dynamics using a classical potential that is derived from the Coulomb interaction between the projectile's charge Ze and the time-dependent total charge density $\rho(R,t)$ of all constituents of the material.

As a prototype model for a correlated material, we consider single-band Hubbard nano clusters with a 2D honeycomb structure, the interparticle distance $a_0 = 1.42\,\text{Å}$ and L sites that have spatial coordinates R_i. With a nearest-neighbor hopping J and an on-site Coulomb interaction U, the cluster Hamiltonian reads

$$H = -J \sum_{\langle i,j\rangle\sigma} c_{i\sigma}^\dagger c_{j\sigma} + U \sum_i \left(n_{i\uparrow} - \tfrac{1}{2}\right)\left(n_{i\downarrow} - \tfrac{1}{2}\right) + \sum_{i\sigma} W_i(t) c_{i\sigma}^\dagger c_{i\sigma}\,, \tag{9}$$

where $n_{i\sigma} = c_{i\sigma}^\dagger c_{i\sigma}$ is the electron density, and $\langle i,j\rangle$ indicates summation over nearest neighbors. In our calculations, we chose the hopping parameter as $J = 2.8\,\text{eV}$, which results from a mapping of *ab-initio* calculations to graphene-type systems in the tight-binding approximation[78,79]. This choice provides a typical setting with a realistic synchronization of the projectile–lattice time scales. Furthermore, the last term of Eq. 9 describes the Coulomb interaction of the lattice electrons with the projectile in terms of a time-dependent on-site energy

$$W_i(t) = -\frac{1}{4\pi\epsilon_0}\frac{Ze^2}{|r(t) - R_i|}\,. \tag{10}$$

Throughout, we consider the case of half filling and measure times in units of $t_0 = \hbar/J$. Inside the KBE, the many-body Hamiltonian (9) translates into a one-particle Hamiltonian

$$\bar{h}_{ij\sigma}(t) = -J\delta_{\langle i,j\rangle} + \left[U\left(\langle n_{i\sigma}(t)\rangle - \tfrac{1}{2}\right) + W_i(t)\right]\delta_{ij}\,. \tag{11}$$

Note that, for Hubbard systems, the Fock terms of the mean field are absent. In addition, we employ the second Born (2B) selfenergy of the form

$$\Sigma_{ij\sigma}^{\text{2B}}(t,t') = \hbar^2 U^2 [G_{ij\sigma}(t,t')]^2 G_{lj\sigma}(t',t)\,, \tag{12}$$

where, in the special case of a "local" selfenergy (local 2B), the site-off-diagonal components are neglected, as mentioned above. The trajectory along which the projectile passes through the cluster is calculated from the potential

$$V(t) = \frac{Ze^2}{4\pi\epsilon_0}\sum_i \frac{\rho(R_i,t)}{|r(t) - R_i|}\,, \tag{13}$$

where $\rho(R_i,t) = -\sum_\sigma \left(\langle n_{i\sigma}(t)\rangle - \frac{1}{2}\right)$ is the total charge density on the cluster, assuming a positive background that results from the atomic cores in a real material. As initial conditions we use $r(t_{-\infty}) = (x_0, y_0, -z_0)$, where z_0 is chosen such that the projectile penetrates the cluster at half the simulation time, and $\mathrm{d}r/\mathrm{d}t(t_{-\infty}) = (0,0,v_0)$, performing calculations for a perpendicular incidence, with the honeycomb cluster located in the xy-plane.

A central observable which characterizes the stopping process is the energy loss of the projectile (P),

$$S = E_{\text{kin}}^{\text{P}}(t_{+\infty}) - E_{\text{kin}}^{\text{P}}(t_{-\infty})\,, \tag{14}$$

where $E_{\text{kin}}^{\text{P}}(t_{-\infty}) \equiv E_{\text{kin},0}^{\text{P}} = \frac{1}{2}mv_0^2$ and $E_{\text{kin}}^{\text{P}}(t_{+\infty})$ denote the initial and final kinetic energies, before and after passing through the cluster, respectively. Further important observables are the different energy contributions on the cluster, i.e., the kinetic, potential and interaction energy:

$$E_{\text{kin}}(t) = \Re\left[-J\sum_{ij}\delta_{\langle i,j\rangle}\rho_{ji}(t)\right], \qquad E_{\text{pot}}(t) = \Re\left[\sum_i W_i(t)\rho_{ii}(t)\right] \quad \text{and} \tag{15}$$

$$E_{\text{int}}(t) = \frac{\mathrm{i}\hbar}{2}\Im\left[\sum_{ij}\int_C \mathrm{d}s\,\Sigma_{ij}(t,s)G_{ji}(s,t^+)\right], \tag{16}$$

where the latter is decomposed into mean field (Hartree–Fock) and correlation energy according to $E_{\text{HF}}(t) = \Re\left[\sum_i U\rho_{ii}(t)\right]$ and $E_{\text{corr}}(t) = E_{\text{int}}(t) - E_{\text{HF}}(t)$. Furthermore, we analyzed the evolution of the local and cluster-averaged double occupation,

$$d_i(t) = \langle n_{i\uparrow}(t) n_{i\downarrow}(t)\rangle = -\frac{\mathrm{i}\hbar}{U}\sum_k\int_C \mathrm{d}s\,\Sigma_{ik}(t,s)G_{ki}(s,t^+)\,, \qquad d_{\text{avg}}(t) = \frac{1}{L}\sum_{i=1}^{L} d_i(t)\,, \tag{17}$$

where spin indices are omitted.

3.2 | Time-resolved energy exchange between projectile and cluster

Below we present numerical results of the KBE coupled to the semiclassical projectile dynamics, as introduced in Ref. 80. We consider two honeycomb clusters that are described by the Hubbard model (9) containing $L = 24$ and $L = 54$ sites, respectively, see Fig. 4 for a sketch of the former. We start by giving an overview of the general dynamical behavior of correlated 2D systems during the impact of a charged particle. For the 54-site cluster, the results are shown in Fig. 2 for the case of a proton, penetrating the lattice at the centroid point C with $\boldsymbol{R}_{\mathrm{C}} = \left(-\frac{1}{6}a_0, -\frac{\sqrt{3}}{3}a_0, 0\right)$. We apply the NEGF approach including the GKBA, as introduced in Sec. 3.1, to study the coupled projectile–lattice dynamics. Thereto, we first generate the correlated ground state of the electrons on the lattice via an adiabatic-switching procedure, where the interaction U of the system is slowly ramped to its final value during the initial time-propagation interval (see Ref.69 for details). We consider the case of $U = 4J$—a configuration that allows for the build-up of correlations. Once the interacting ground state is reached, the projectile dynamics starts by solving the coupled equations (9) to (13). For a broad range of projectile energies, $10^{-1}\,\mathrm{keV/u} < E^{\mathrm{P}}_{\mathrm{kin},0} < 10^{3}\,\mathrm{keV/u}$, we compute the dynamical evolution of relevant energies of both, the lattice electrons and the proton. The results are shown in Fig. 2 . For better comparability, all quantities are plotted as a function of the time-dependent projectile position $z^{\mathrm{P}}(t)$. To further illustrate the dependence of the relevant observables on the ion impact energy we show slices for three different ion–surface distances, $z^{\mathrm{P}}/a_0 = 0, 2.5, 5$, corresponding to the impact time ($z^{\mathrm{P}} = 0$) and two slightly later times, in Fig. 3 .

Consider first the *kinetic energy of the projectile* that is shown in part (e) of Figs. 2 and 3 . The energy loss of the projectile to the cluster can be seen from a vertical cut through Fig. 2 (e) at large z^{P}. One clearly recognizes the familiar bell-shaped dependence on the impact energy with a single peak around 10 keV/u. On the other hand, looking at horizontal cuts provides the time dependence of the proton energy: before the impact (negative z^{P}) the proton gains energy because it is attracted by the electrons of the cluster, whereas after the impact the proton loses energy to the electrons (more than it had gained before), see also part (e) of Fig. 3 . A general discussion of this behavior has been given in Ref. 13. Here we provide more details of the physics including a breakup of the energy gain of the electrons into different contributions: potential energy in the field of the projectile, kinetic energy, mean-field energy and correlation energy.

The *potential energy of the cluster electrons* in the Coulomb field of the projectile, Eq. (15), is shown in Fig. 2 (a). Whereas, in the absence of the projectile this energy is zero, during the impact the attraction of the electrons towards the projectile impact point gives rise to a large (negative) energy—electrons are confined in a potential well centered at the impact point. For each projectile energy, $E^{\mathrm{P}}_{\mathrm{kin},0}$, the potential energy is perfectly symmetric with respect to the impact point $z^{\mathrm{P}} = 0$. This demonstrates that there is no drift of the ion in x- and y-direction during the penetration process. Next consider the *kinetic energy* of the electrons, Fig. 2 (c), and compare it to the kinetic energy of the projectile, Fig. 2 (e). For any vertical cut through the figures (constant $z^{\mathrm{P}} > 0$) the two energies are essentially mirror images of each other. The maximum energy reduction of the projectile (maximal stopping) is observed slightly below $E^{\mathrm{P}}_{\mathrm{kin},0} = 10\,\mathrm{keV/u}$, exactly where the electrons experience the highest kinetic-energy gain. This is even more clearly visible in blue and green curves in Fig. 3 (c) and (e). Figure 2 (b) shows the *Hartree–Fock part of the interaction energy* of the electrons. It is directly proportional to the electron density, cf. Eq. (16) and, thus, illustrates the density response to the projectile. Note the striking difference in the two limiting cases of low and high ion energy, respectively: for low $E^{\mathrm{P}}_{\mathrm{kin},0}$, the electron density adiabatically follows the external excitation, leading to a symmetric bell-shaped curve, similar to E_{pot}. In contrast, for high-energy ions, the interaction time is too short for the electronic system to respond, therefore the density and, thus, E_{HF} do not change significantly—even during the particle impact. The physics inbetween these two limits is dominated by an increasingly delayed and broadened response of the electron density, due to the build up of electron–electron correlations. The same trends are seen also in Fig. 3 (c): for example the red curve demonstrates the reduction of the electronic density response with increasing projectile speed. Consider now the *correlation energy* of the electrons, E_{corr}, Eq. (16), and the closely related average doublon number, d_{avg}, Eq. (17), that are displayed in Figs. 2 (d) and (f), respectively. Both quantities show a very similar behavior that resembles that of the Hartree–Fock energy, E_{HF}, cf. figure part (b). Thus, both quantities mainly following the evolution of the density, as well, which is also seen in Fig. 3 , compare parts (d, f) to part (b).

The time-dependent re-distribution of the energy gained by the electrons between kinetic, mean-field and correlation energy can be clearly seen in Fig. 3 (b-d), compare the red and green curves. When the projectile departs towards positive z^{P}, the kinetic energy always increases because the potential well that has trapped the electrons is removed. At the same time, Hartree–Fock and correlation energy decrease, for impact energies below 10 keV/u, cf. parts (b,d) of Fig. 3 . In contrast, for impact energies exceeding approximately 10 keV/u (25 keV/u) the Hartree–Fock (correlation) energy increase.

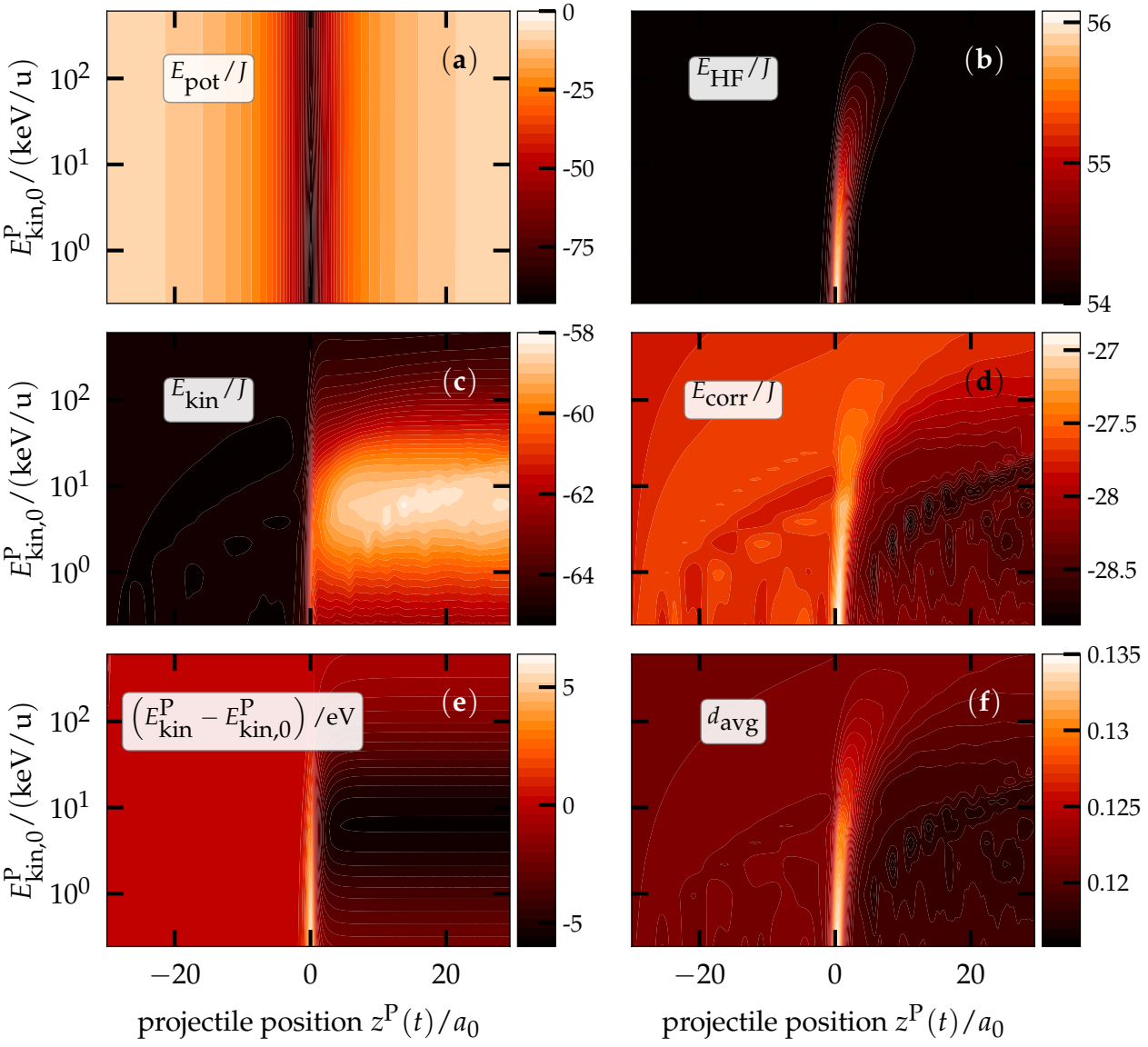

FIGURE 2 Evolution of relevant energies during the impact of a proton at point C [cf. Fig. 4] on a 54−site honeycomb cluster at correlation strength $U = 4J$ for different initial kinetic energies in the range 10^{-1} keV/u $< E^{\mathrm{P}}_{\mathrm{kin},0} < 10^3$ keV/u, indicated on the y-axis. The x-axis contains the current height of the proton, $z^{\mathrm{P}}(t)$, (impacting from the left) above the cluster plane. Since the projectile velocity is almost constant, the height is a measure of time. **(a)**: potential energy, **(b)**: Hartree–Fock energy, **(c)**: kinetic energy, **(d)**: correlation energy, and **(f)**: average double occupation of the lattice electrons; **(e)**: kinetic energy loss of the projectile. The color scale is shown to the right of each figure. To ease the analysis of the data, three vertical cuts at $z^{\mathrm{P}} = 0;\ 2.5;\ 5$ through each graph are shown in Fig. 3 .

3.3 | Correlated-energy dissipation for impact energies below 1keV

In this section, we perform additional simulations for an $L = 24$-site honeycomb cluster (cf. visualization in Fig. 4), where we focus, in particular, on correlation effects at small proton energies. To reach sufficiently long simulation times, in this case, we do not perform an adiabatic switching on of the interaction U but start from the Hartree ground state, for the inclusion of a correlated initial state, see Refs. 81 and 82. In this case the proton impact should occur only after the initial transient dynamics which are caused by the sudden (nonadiabatic) switch on of the 2B selfenergy. These transient dynamics also change the initial Hartree double occupation $d_{\mathrm{avg}}(t_{-\infty}) = \frac{1}{2L}\sum_{i\sigma}\langle n_{i\sigma}(t_{-\infty})\rangle = 0.25$ to some smaller value [for details see Ref. 80]. Extending the

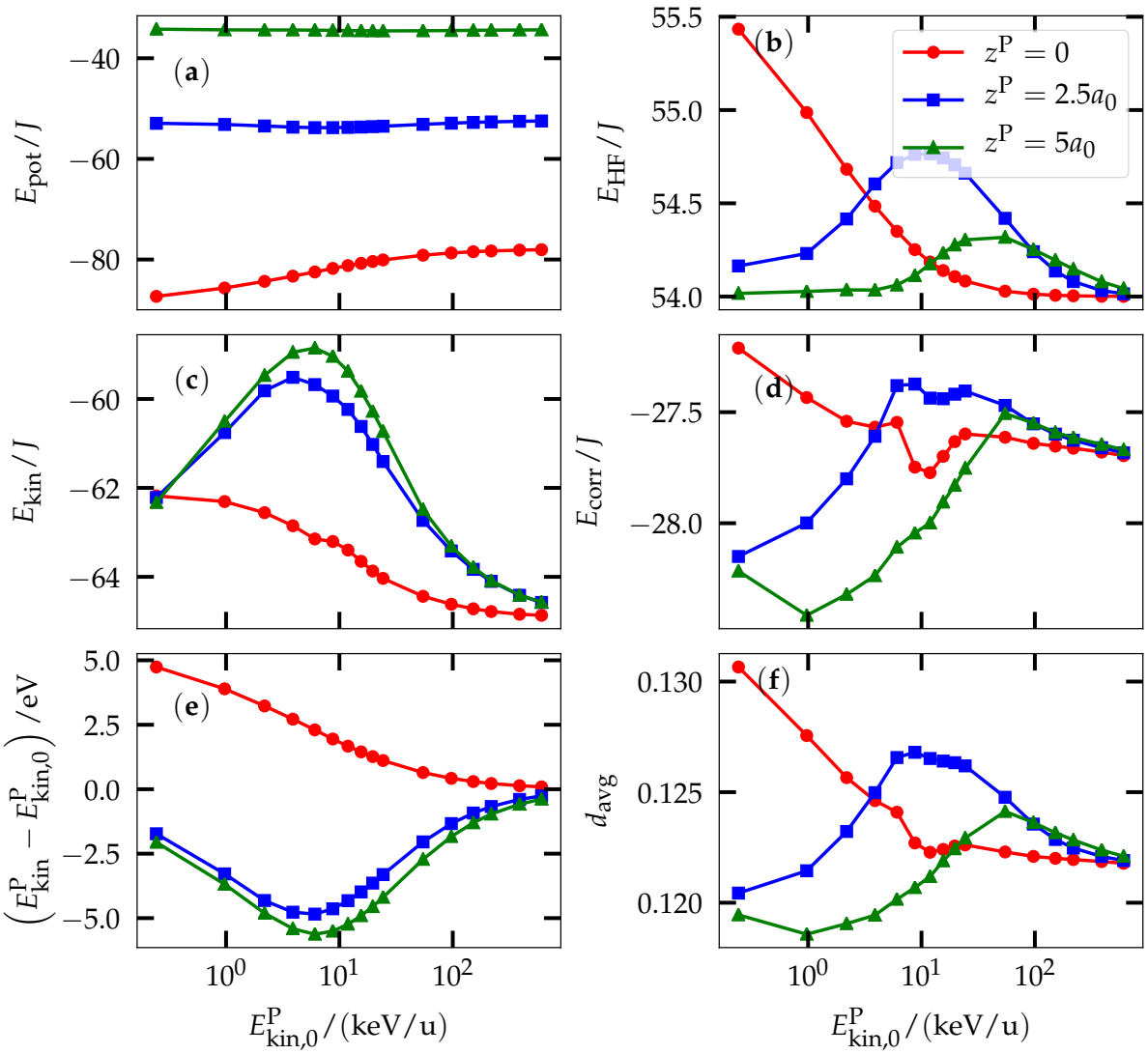

FIGURE 3 Same as Fig. 2 , but for three cuts at fixed values z^{P} of the proton coordinate (height above the plane): in the cluster plane ($z^{\mathrm{P}} = 0$, red line) and two distances after the impact (blue and green), see inset of top right figure.

work of Ref. 80, we consider in the following two different initial positions of the proton: the points S (cluster center, blue) and C (centroid point, red) as sketched in Fig. 4 .

Figures 4 (a) and (b) show the energy loss in a broad range of proton energies between 0.05 and 25 keV/u for three different values of the interaction strength $U/J \leq 4$. For the point C (red curves), the peak position of the energy loss is located roughly around 10 keV/u, while, for the point S (blue curves), the maximum of the stopping power varies between 4 keV/u ($U = 0$) and 15 keV/u ($U/J = 4$). Generally, we observe that, in the investigated regime, an increase of the interaction strength U leads to a smaller energy loss for fixed impact parameters. Moreover, when the energy is decreased below 0.1 keV/u, the energy loss rapidly vanishes, in a mean-field description, due to a rather instantaneous change of the charge density on the cluster, which we attribute to the onset of the adiabatic-response regime.

In the next step, we examine the influence of electron–electron correlations on the energy loss. In the 2B approximation for a moderate interaction strength of $U/J = 4$, we find clear deviations from the Hartree results. Around $E^{\mathrm{P}}_{\mathrm{kin},0} = 1$ keV/u, the correlated result for the stopping power significantly exceeds the Hartree result, for the starting point C, while for the point S the correlated results remain close to the mean-field result. When the impact energy is further reduced the situation changes. For the impact point C correlated and uncorrelated simulations do not differ systematically. In contrast, for impact point S the

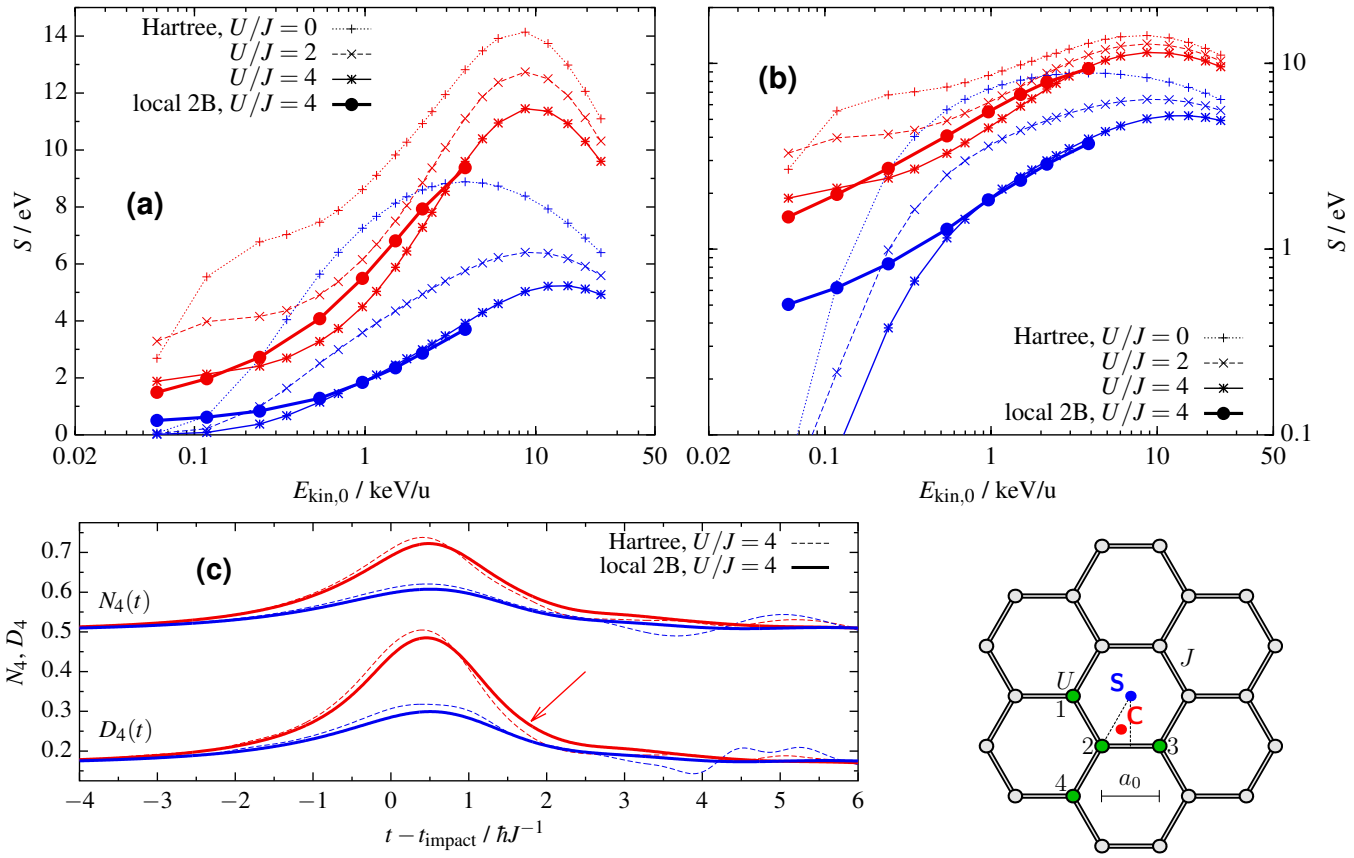

FIGURE 4 **(a)** and **(b)**: Energy loss $S(E^{\mathrm{P}}_{\mathrm{kin},0})$ of a proton passing through a 24-site honeycomb cluster ($J = 2.8\,\mathrm{eV}$, $a_0 = 1.42\,\text{Å}$.) at three correlation strengths $U/J = 0, 2, 4$, for two different impact points marked in the bottom right figure: C $\left(-a_0/6, -a_0/\sqrt{3}, 0\right)$, red lines) and S (cluster center, blue lines). Figure (b) shows the same data as (a) on a logarithmic scale to better resolve the low-energy behavior. For $U/J = 4$, we include, in addition to the Hartree calculations, results obtained in the local second-order Born approximation (local 2B). Note that, at impact energies below 2 keV, electron–electron correlations tend to increase the energy loss compared to the mean-field result. **(c)**: Time evolution of the density $N_4(t)$ and double occupation $D_4(t)$, as defined in the text (averages over the four green sites in the bottom right figure), for the impact energy $E^{\mathrm{P}}_{\mathrm{kin},0} = 1\mathrm{keV}$. The red arrow marks the ion-induced doublon excitation that is observed in the correlated simulations.

correlated calculation leads to a significantly increased energy loss compared to the mean-field simulation. Moreover, at and below 0.2 keV/u, the energy loss seems to be dominated by correlation effects, as the mean-field results rapidly vanish, for point S. This low-energy behavior needs further investigation since here also effects beyond the second-Born approximation might become important.

Let us now return to the impact energy $E^{\mathrm{P}}_{\mathrm{kin},0} = 1\,\mathrm{keV/u}$. We expect that the increased energy loss obtained in the local 2B calculations for the starting point C, is a consequence of enhanced doublon formation on the cluster, triggered by the interaction with the proton along the excitation protocol discussed in Ref. 14. This protocol connects single-electron and doublon states in a strongly correlated Hubbard model via nonadiabatic Landau–Zener transitions. As an indication that such excitations play a crucial role, we mention that, for the case C, the maximum value of the interaction energy with the proton at the nearest lattice site, $|W_{i=2}(t)|$, is about twice as large as the electron–electron interaction strength U, which was found to be the optimum condition for ion-induced doublon excitation in Ref. 14. In contrast, this energy is of the order of U, for the impact point S. For cases where the maximum value of the interaction with the proton is smaller, $|W| \lesssim U$, doublon production should be not as efficient as for on-site energies $W \gtrsim 2U$, cf. Refs. 14 and 77.

Additional support for these arguments is obtained from an analysis of the time evolution of the electron density and double occupation on the cluster. In Fig. 4 (c), we show two quantities: $N_4(t) = \frac{1}{4}\sum_{\alpha=1}^{4}\langle n_{\alpha\sigma}(t)\rangle$ and $D_4(t) = \frac{1}{4}\sum_{\alpha=1}^{4} d_\alpha(t)$, i.e., the density and doublon number averaged over the four sites that are nearest to the impact point C, cf. the green sites labeled 1 to

4 in the cluster sketch of Fig. 4 . We observe that, after the impact, the relaxation of the density towards the equilibrium value $N_4 = \langle n_{i\sigma} \rangle = 0.5$ is slightly different for the cases C and S. In the former case, the density in 2B approximation remains larger than the Hartree result whereas, in the latter case the second-Born result is slightly lower, at least up to the time $t - t_{\text{impact}} \approx 2.5\hbar J^{-1}$. From the quantity D_4 we find that this difference in the evolution of the densities is associated with a larger doublon number after the impact, in a correlated simulation, for the case C, see the red arrow. Also, note, that we have computed D_4 in Hartree approximation with the full mean-field NEGF $G(t, t')$ according to Eq. (17) instead of evaluating just the uncorrelated part $D_4^{\text{uncorr}} = \frac{1}{4} \sum_{\alpha=1}^{4} \langle n_{\alpha\sigma}(t) \rangle^2$, that has the equilibrium limit $D_4(t_{-\infty}) = 0.25$.

Even though the effect of doublon excitation is not strong, in the present case, recent simulations have confirmed the importance of this effect, as will be discussed in Sec. 4.

4 | CONCLUSIONS AND OUTLOOK

In this article we presented new results of time-dependent quantum simulations for the dynamics of ions near a solid surface. Such processes are of prime importance for the interaction of plasmas with solids where many questions remain poorly understood. We focused on two important aspects of ion stopping in nanoscale solid systems exposed to low-energy projectiles: 1) the charge transfer from the surface to the projectile and 2) the modification of the projectile energy loss in case of a target material with strong electronic correlations. While the former problem was studied using time-dependent DFT simulations, the latter one was studied using nonequilibrium Green functions simulations for small graphene-type Hubbard clusters. The results for the two problems are summarized below before we discuss future developments.

In our TDDFT simulations we have used an adiabatic GGA for the exchange–correlation potential and, thus, restricted ourselves to a resonant charge-transfer process. A proton incident on an Al(111) surface serves as a well-established model system, which has been studied intensely for a long time using model Hamiltonians[24,27–30]. The strength of TDDFT-MD lies in the *ab-initio* material-specific description of the time-dependent charge and energy transfer and the screening. Tunneling rates differ from estimates from electronic ground-state theory. Limitations of the approach are due to the adiabatic approximation for exchange and correlation plus the semilocal approximation applied to the exchange–correlation energy functional of ground-state DFT, and improvements pose an open problem.

In our NEGF simulations we have concentrated on electronic correlation effects in the stopping of ions. We have confirmed that, at impact energies below 1keV correlations tend to increase the energy transfer to the target, compared to an uncorrelated (Hartree) simulation. Among the possible mechanisms is the excitation of doublons in the target. In Ref. 77 it was shown that, for a proper choice of impact energy, and for a more strongly-coupled hexagon cluster ($U/J \geq 10$) of size $L = 12$ an ion impacting in the cluster center may excite a large doublon number that does not decay after the projectile has left. Moreover, it was shown in Refs. 14 and 77 that, in the case of multiple ion impacts, the doublon number can be increased further.

Let us now discuss the combined treatment of the two effects. Even though charge transfer is most likely not relevant for the kinetic energy loss of the projectile, it may well affect the electronic processes in the target, including doublon excitations. Answering these questions, though, requires a combination of the two simulation methods. However, presently none of the two methods is capable of incorporating the missing effect. Present approximations to the exchange–correlation potential in TDDFT simulations do not describe strongly correlated systems and, thus, cannot treat doublon formation in the target. On the other hand, NEGF simulations of charge transfer have recently been attempted for simple model systems (1D Hubbard chains) in Refs. 77 and 12. However, these simulations did not include a realistic treatment of the impacting ion. Here, a combination with TDDFT could be the basis for major progress. A possible combination could be via a Newns–Anderson model for the projectile where TDDFT provides selfconsistent model parameters. A second promising combination of the two methods consists in the derivation of improved exchange–correlation functionals for TDDFT that include finite-temperature effects[83,84] and their benchmarking by NEGF simulations. This will be particularly important for the treatment of Auger-type processes in the interaction of an ion or atom with the surface which are straightforwardly described within NEGF already with second-order Born selfenergies, e.g. Refs. 12 and 85. These combinations of TDDFT and NEGF are expected to be of high importance for the development of accurate simulations of low-temperature plasma–surface interaction. Moreover, such combinations should also be of high interest for other fields including surface physics and chemistry.

ACKNOWLEDGMENTS

Helpful discussions with A. Dávila are gratefully acknowledged. We further acknowledge computing time at the Rechenzentrum of Kiel University where the calculations have been carried out.

References

[1] I. Nagy, B. Apagyi, *Phys. Rev. A* **1998**, *58*, R1653–R1656.

[2] J. M. Pitarke, R. H. Ritchie, P. M. Echenique, *Phys. Rev. B* **1995**, *52*, 13883–13902.

[3] Tobias Dornheim, Simon Groth, Jan Vorberger, Michael Bonitz, *Phys. Rev. Lett.* **2018**, *121*, 255001.

[4] M. Quijada, A. G. Borisov, I. Nagy, R. Díez Muiño, P. M. Echenique, *Phys. Rev. A* **2007**, *75*, 042902.

[5] Ari Ojanperä, Arkady V. Krasheninnikov, Martti Puska, *Phys. Rev. B* **2014**, *89*, 035120.

[6] S. Zhao, W. Kang, J. Xue, X. Zhang, P. Zhang, *J. Phys. Condens. Matter* **2015**, *27*, 025401.

[7] James F. Ziegler, M.D. Ziegler, J.P. Biersack, *Nuclear Instruments and Methods in Physics Research Section B: Beam Interactions with Materials and Atoms* **2010**, *268* (11), 1818–1823, 19th International Conference on Ion Beam Analysis.

[8] M. Bonitz, D. Kremp, S. Kosse, D.C. Scott, W.D. Kraeft, in *Proceedings of the XXII. Intern. Conference on Phenomena in Ionized Gases*, Hoboken, NJ, USA, **1995**, pp. –.

[9] M. Bonitz, D. Kremp, S. Kosse, D.C. Scott, W.D. Kraeft, in *Physics of strongly coupled plasmas*, World Scientific, **1996**, p. 117.

[10] A. B. Zylstra, J. A. Frenje, P. E. Grabowski, C. K. Li, G. W. Collins, P. Fitzsimmons, S. Glenzer, F. Graziani, S. B. Hansen, S. X. Hu, M. Gatu Johnson, P. Keiter, H. Reynolds, J. R. Rygg, F. H. Séguin, R. D. Petrasso, *Phys. Rev. Lett.* **2015**, *114*, 215002.

[11] D. Kremp, M. Schlanges, W.D. Kraeft, *Quantum Statistics of Nonideal Plasmas*, Springer, **2005**.

[12] M Bonitz, A V Filinov, JW Abraham, K Balzer, H Kaehlert, E Pehlke, F X Bronold, M Pamperin, M Becker, D Loffhagen, H Fehske, *Front. Chem. Science and Engineering* **2018**, accepted for publication.

[13] Karsten Balzer, Niclas Schlünzen, Michael Bonitz, *Phys. Rev. B* **2016**, *94*, 245118.

[14] K Balzer, M Rasmussen, N Schlünzen, J P Joost, M Bonitz, *Phys. Rev. Lett., arXiv:1801.05267* **2018**, in press.

[15] Miguel A.L. Marques, Alberto Castro, George F. Bertsch, Angel Rubio, *Computer Physics Communications* **2003**, *151* (1), 60 – 78.

[16] Alberto Castro, Heiko Appel, Micael Oliveira, Carlo A. Rozzi, Xavier Andrade, Florian Lorenzen, M. A. L. Marques, E. K. U. Gross, Angel Rubio, *physica status solidi (b)* **2006**, *243* (11), 2465–2488.

[17] Xavier Andrade, David Strubbe, Umberto De Giovannini, Ask Hjorth Larsen, Micael J. T. Oliveira, Joseba Alberdi-Rodriguez, Alejandro Varas, Iris Theophilou, Nicole Helbig, Matthieu J. Verstraete, Lorenzo Stella, Fernando Nogueira, Al/'an Aspuru-Guzik, Alberto Castro, Miguel A. Marques, Angel Rubio, *Phys. Chem. Chem. Phys.* **2015**, *17*, 31371.

[18] Dominik Marx, Jürg Hutter, *Ab Initio Molecular Dynamics: Basic Theory and Advanced Methods*, Cambridge University Press, **2009**.

[19] M. A. L. Marques, C. A. Ullrich, F. Nogueira, A. Rubio, K. Burke, E. K. U. Gross (Eds:), *Time-Dependent Density Functional Theory*, Vol. 706 of *Lecture Notes in Physics*, Springer, **2006**.

[20] Miguel A. L. Marques, Neepa T. Maitra, Fernando M. S. Nogueira, Eberhard K. U. Gross, A. Rubio (Eds:), *Fundamentals of Time-Dependent Density Functional Theory*, Vol. 837 of *Lecture Notes in Physics*, Springer, **2012**.

[21] M. Lindenblatt, E. Pehlke, A. Duvenbeck, B. Rethfeld, A. Wucher, *Nuclear Instruments and Methods in Physics Research Section B: Beam Interactions with Materials and Atoms* **2006**, *246* (2), 333 – 339.

[22] R. Nagano, K. Yabana, T. Tazawa, Y. Abe, *Phys. Rev. A* **2000**, *62*, 062721.

[23] V. Kapoor, *Phys. Rev. A* **2016**, *93*, 063408.

[24] J. Merino, N. Lorente, M. Yu. Gusev, F. Flores, M. Maazouz, L. Guillemot, V. A. Esaulov, *Phys. Rev. B* **1998**, *57*, 1947–1956.

[25] R. Zimny, Z.L. Mišković, N.N. Nedeljković, Lj.D. Nedeljković, *Surface Science* **1991**, *255* (1), 135 – 156.

[26] H. Jouin, F. A. Gutierrez, *Phys. Rev. A* **2011**, *84*, 014901.

[27] J. Merino, N. Lorente, P. Pou, F. Flores, *Phys. Rev. B* **1996**, *54*, 10959–10969.

[28] J. Merino, N. Lorente, F. Flores, M.Yu. Gusev, *Nuclear Instruments and Methods in Physics Research Section B: Beam Interactions with Materials and Atoms* **1997**, *125* (1), 288 – 292, Inelastic Ion-Surface Collisions.

[29] M. C. Torralba, P. G. Bolcatto, E. C. Goldberg, *Phys. Rev. B* **2003**, *68*, 075406.

[30] David C. Langreth, P. Nordlander, *Phys. Rev. B* **1991**, *43*, 2541–2557.

[31] Christopher L. Moss, Christine M. Isborn, Xiaosong Li, *Phys. Rev. A* **2009**, *80*, 024503.

[32] A. Castro, M. Isla, José I. Martínez, J. A. Alonso, *Chemical Physics* **2012**, *399*, 130.

[33] Arkady V. Krasheninnikov, Yoshiyuki Miyamoto, David Tománek, *Phys. Rev. Lett.* **2007**, *99*, 016104.

[34] Rodrigo Seraide, Mario A. Bernal, Gustavo Brunetto, Umberto de Giovannini, Angel Rubio, *The Journal of Physical Chemistry B* **2017**, *121* (30), 7276–7283.

[35] Sergiy Bubin, Bin Wang, S. Pantelides, Kálmán Varga, *Phys. Rev. B* **2012**, *85*, 235435.

[36] Shijun Zhao, Wei Kang, Jianming Xue, Xitong Zhang, Ping Zhang, *Journal of Physics: Condensed Matter* **2015**, *27* (2), 025401.

[37] Zhi Wang, Shu-Shen Li, Lin-Wang Wang, *Phys. Rev. Lett.* **2015**, *114*, 063004.

[38] Neepa T Maitra, *Journal of Physics: Condensed Matter* **2017**, *29* (42), 423001.

[39] Shijun Zhao, Wei Kang, Jianming Xue, Xitong Zhang, Ping Zhang, *Physics Letters A* **2015**, *379*, 319.

[40] John P. Perdew, Kieron Burke, Matthias Ernzerhof, *Phys. Rev. Lett.* **1996**, *77*, 3865.

[41] N. Trouiller, J. L. Martins, *Phys. Rev. B* **1991**, *43*, 1993.

[42] Martin Fuchs, Matthias Scheffler, *Computer Physics Communications* **1999**, *119* (1), 67 – 98.

[43] Maxim Tafipolsky, Rochus Schmid, *The Journal of Chemical Physics* **2006**, *124* (17), 174102.

[44] M. Methfessel, A. T. Paxton, *Phys. Rev. B* **1989**, *40*, 3616–3621.

[45] Guillermo Avendaño Franco, Ph.D. thesis, Université Catholique de Louvain, **2013**.

[46] Alberto Castro, Miguel A. L. Marques, Angel Rubio, *The Journal of Chemical Physics* **2004**, *121* (8), 3425–3433.

[47] William Humphrey, Andrew Dalke, Klaus Schulten, *Journal of Molecular Graphics* **1996**, *14*, 33–38.

[48] T. Noritake, M. Aoki, S. Towata, Y. Seno, Y. Hirose, E. Nishibori, M. Takata, M. Sakata, *Applied Physics Letters* **2002**, *81* (11), 2008–2010.

[49] M. Fuchs, Y.-M. Niquet, X. Gonze, K. Burke, *The Journal of Chemical Physics* **2005**, *122* (9), 094116.

[50] O. Gunnarsson, B. I. Lundqvist, *Phys. Rev. B* **1976**, *13*, 4274–4298.

[51] M. Lindenblatt, E. Pehlke, *Phys. Rev. Lett.* **2006**, *97*, 216101.

[52] M. S. Mizielinski, D. M. Bird, M. Persson, S. Holloway, *J. Chem. Phys.* **2005**, *122*, 084710.

[53] M. A. Cazalilla, N. Lorente, R. Díez Muiño, J.-P. Gauyacq, D. Teillet-Billy, P. M. Echenique, *Phys. Rev. B* **1998**, *58*, 13991–14006.

[54] Diego Valdés, E. C. Goldberg, J. M. Blanco, R. C. Monreal, *Phys. Rev. B* **2005**, *71*, 245417.

[55] N. P. Wang, Evelina A. García, R. Monreal, F. Flores, E. C. Goldberg, H. H. Brongersma, P. Bauer, *Phys. Rev. A* **2001**, *64*, 012901.

[56] M Pamperin, F X Bronold, H Fehske, *Plasma Sources Science and Technology* **2018**, *27* (8), 084003.

[57] M. Lindenblatt, J. van Heys, E. Pehlke, *Surface Science* **2006**, *600* (18), 3624 – 3628.

[58] H. Winter, *Journal of Physics: Condensed Matter* **1996**, *8* (49), 10149.

[59] E.V. Chulkov, V.M. Silkin, P.M. Echenique, *Surface Science* **1999**, *437* (3), 330 – 352.

[60] Alfredo A. Correa, Jorge Kohanoff, Emilio Artacho, Daniel Sánchez-Portal, Alfredo Caro, *Phys. Rev. Lett.* **2012**, *108*, 213201.

[61] André Schleife, Yosuke Kanai, Alfredo A. Correa, *Phys. Rev. B* **2015**, *91*, 014306.

[62] M. Quijada, A. G. Borisov, I. Nagy, R. Díez Muiño, P. M. Echenique, *Phys. Rev. A* **2007**, *75*, 042902.

[63] I. Campillo, J. M. Pitarke, A. G. Eguiluz, *Phys. Rev. B* **1998**, *58*, 10307–10314.

[64] Abdullah Atef Shukri, Fabien Bruneval, Lucia Reining, *Phys. Rev. B* **2016**, *93*, 035128.

[65] M.J. Berger, J.S. Coursey, M.A. Zucker, J. Chang, *Stopping-Power and Range Tables for Electrons, Protons, and Helium Ions*, https://dx.doi.org/10.18434/T4NC7P, **1999**.

[66] G. Stefanucci, R. van Leeuwen, *Nonequilibrium Many-Body Theory of Quantum Systems*, Cambridge University Press, Cambridge, **2013**.

[67] L.P. Kadanoff, G. Baym, *Quantum Statistical Mechanics*, Benjamin, New York, **1962**.

[68] K. Balzer, M. Bonitz, *Nonequilibrium Green's Functions Approach to Inhomogeneous Systems*, Springer, Berlin Heidelberg, **2013**.

[69] N. Schlünzen, M. Bonitz, *Contributions to Plasma Physics* **2016**, *56* (1), 5–91.

[70] L.V. Keldysh, *Soviet Phys. JETP* **1965**, *20*, 1018, (*Zh. Eksp. Teor. Fiz.* **1964**, *47*, 1515).

[71] M. Bonitz, A.P. Jauho, M. Sadovskii, S. Tikhodeev, *physica status solidi (b)* **2018**, , submitted for publication.

[72] N. Schlünzen, S. Hermanns, M. Bonitz, C. Verdozzi, *Phys. Rev. B* **2016**, *93*, 035107.

[73] N. Schlünzen, J.-P. Joost, F. Heidrich-Meisner, M. Bonitz, *Phys. Rev. B* **2017**, *95*, 165139.

[74] P. Lipavský, V. Špička, B. Velický, *Phys. Rev. B* **1986**, *34*, 6933–6942.

[75] S Hermanns, K Balzer, M Bonitz, *Physica Scripta* **2012**, *2012* (T151), 014036.

[76] K. Balzer, M. Eckstein, *Phys. Rev. B* **2014**, *89*, 035148.

[77] M Bonitz, K Balzer, N Schlünzen, M Rasmussen, J-P Joost, *physica status solidi (b)* **2018**, in press.

[78] S. Reich, J. Maultzsch, C. Thomsen, P. Ordejón, *Phys. Rev. B* **2002**, *66*, 035412.

[79] Jan-Philip Joost, Niclas Schlünzen, Michael Bonitz, *Phys. Status Solidi B* **2019**, *0* (0), 1800498.

[80] K. Balzer, N. Schlünzen, M. Bonitz, *Phys. Rev. B* **2016**, *94*, 245118.

[81] Semkat D., D. Kremp, M. Bonitz, *Phys. Rev. E* **1999**, **59**, 1557.

[82] D. Semkat, D. Kremp, M. Bonitz, *J. Math. Phys.* **2000**, **41** (11), 7458–7467.

[83] Tobias Dornheim, Simon Groth, Travis Sjostrom, Fionn D. Malone, W. M. C. Foulkes, Michael Bonitz, *Phys. Rev. Lett.* **2016**, *117*, 156403.

[84] Tobias Dornheim, Simon Groth, Michael Bonitz, *Physics Reports* **2018**, *744*, 1–86.

[85] F. Covito, E. Perfetto, A. Rubio, G. Stefanucci, *Phys. Rev. A* **2018**, *97*, 061401.